

Adjustment of Dissipative Terms to Improve Two and Three-Dimensional Euler Flow Solutions

SEYED SAIED BAHRAINIAN

Department of Mechanical Engineering

Shahid Chamran University

AHWAZ, IRAN

bahrainian@scu.ac.ir

Abstract: - The Euler equations are a set of non-dissipative hyperbolic conservation laws that can become unstable near regions of severe pressure variation. To prevent oscillations near shockwaves, these equations require artificial dissipation terms to be added to the discretized equations. A combination of first-order and third-order dissipative terms control the stability of the flow solutions. The assigned magnitude of these dissipative terms can have a direct effect on the quality of the flow solution. To examine these effects, subsonic and transonic solutions of the Euler equations for a flow passed a circular cylinder has been investigated. Triangular and tetrahedral unstructured grids were employed to discretize the computational domain. Unsteady Euler equations are then marched through time to reach a steady solution using a modified Runge-Kutta scheme. Optimal values of the dissipative terms were investigated for several flow conditions. For example, at a free stream Mach number of 0.45 strong shock waves were captured on the cylinder by using values of 0.25 and 0.0039 for the first-order and third-order dissipative terms. In addition to the shock capturing effect, it has been shown that smooth pressure coefficients can be obtained with the proper values for the dissipative terms.

Key-Words: - Artificial Dissipation - Unstructured Grids - Finite volume – Euler Equations - Shock capturing

1 Introduction

The conservative form of the Euler equations can describe flow conditions for any given inviscid flow. But, the discretized representations of these equations contain errors. These errors are due to numerical approximation and can cause solution instability. Solution instability of the discretized Euler equations can occur near regions of high pressure gradients. These unstable regions include locations of flow stagnation or presence of shock waves. Stagnation points or shock waves can introduce unwanted oscillations into the flow field. To damp oscillations for solution stability, the Euler equations should be modified by adding extra dissipation terms. The main objective of this study is to introduce proper integer values to control the amount of dissipation added for solution stability.

In numerical view point, dissipative terms are mathematical functions that are based on the flow variables. The proper representation of these functions can have direct effect on capturing flow phenomena in regions of instability. For example, to numerically capture a shock wave on a wing, the correct amount of dissipation must be added to the Euler equations in the form of adjustable dissipation coefficients. An under value of added dissipation can cause solution instabilities due to the presence

of undamped shock oscillations. On the other hand, an over value of added dissipation may over damp all the oscillations and instabilities causing the flow solution to diverge from their steady state conditions. The over damping can at best give the incorrect location of the shocks.

Numerically, dissipation functions are added to the Euler equations in the form of dissipation fluxes. These fluxes are described based on the derivatives of flow variables. A third order artificial viscosity has been applied by MacCormak and Baldwin [1], whereby artificial viscosity is made proportional to second derivative of the pressure field in order to enhance the effect of dissipation in the presence of strong pressure gradients and to reduce it in the smooth flow regions (c.f. Hirsch [2]). Another form of artificial viscosity, introduced by Steger [3], is based on the addition of higher-order derivatives in numerical schemes. Jameson and others apply a blend of expressions with excellent shock capturing properties [4, 5].

Here, a pressure sensor adapted from Stolcis and Johnston [7] is used with unstructured grids to solve inviscid flow around a circular cylinder. The aim of these solutions was to investigate and demonstrate the effect of dissipative terms on the quality of two- and three dimensional Euler flow solutions.

2 Computational Grid Generation

The space discretization of the examples presented in this paper makes use of an in-house grid generator. The grid generator is based on a novel algorithm that can generate triangular or tetrahedral unstructured grids. For simplicity and ease of comparisons, triangular meshes in 2-dimensional space are generated for a circular cylinder section. To show consistency with 3-dimensional space, sample tetrahedral grid and solutions are also given for a circular cylinder attached to a plane-of-symmetry.

Grid refinement is based on a combination of point insertion and cell-subdivision methods. An edge-based and a cell-based connectivity matrix were employed simultaneously to prevent searches through the list of edges. The art of this grid generation algorithm is in its geometry movement capability. The algorithm starts with a very coarse initial grid. This initial grid which can be constructed with a few edges is shown in Fig. 1(a). The solid boundary which is initially represented with four edges is refined and moved to fit a circular geometry. The final computational grid output around a circular section is shown in Fig. 1(b).

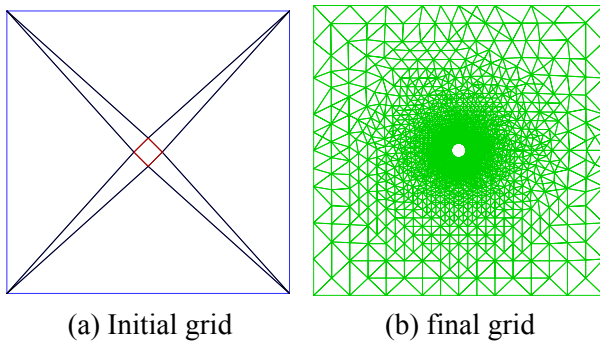


Fig. 1 Grid generation procedure for triangular cells around a cylinder section for two-dimensional cases

The computational grid of Fig. 1 has been used to obtain flow solutions for all of the two-dimensional cases presented in this work. It should be noted that only a diagonal edge swapping procedure has been used to improve the quality of the two-dimensional unstructured grids [10].

Similar approach is taken for the generation of three dimensional tetrahedral cells around a circular cylinder attached to a plane-of-symmetry, and is detailed in Fig. 2. The initial three dimensional tetrahedral grids shown in Figs 2 (a) and (b) have been produced by decomposing hexahedral cells [11]. This initial tetrahedral grid consists of 8 plane-of-symmetry faces, 10 surface geometry faces, 46

interior faces, and 10 outer-boundary faces giving a total of 74 triangular faces [11]. Final computational tetrahedral grids are shown in Figs 2 (d), (e), and (f). This final grid has been employed to obtain all of the three dimensional flow solutions presented in the proceeding sections.

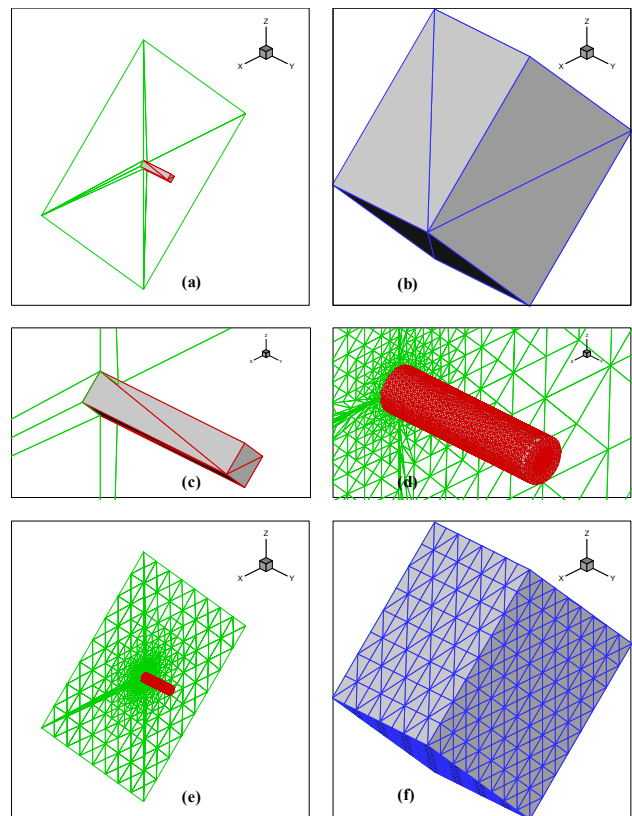


Fig. 2 Computational grid output for a circular cylinder $D = 1$, $L = 4$, where: (a) and (b) show the initial grid, (c) and (d) show close views of initial and final surface faces, (e) and (d) show final plane-of-symmetry, surface, and outer-boundary faces

3 The Euler Equations

From a physical-mathematical point of view the Euler equations can be viewed as the limit of the Navier-Stokes equations for vanishing diffusion effects. If we neglect viscosity and heat conduction terms in the Navier-Stokes equations, their inviscid form known as the Euler equations are obtained. The three-dimensional Euler equations in Cartesian coordinates can be written as:

$$\frac{\partial \mathbf{W}}{\partial t} + \frac{\partial \mathbf{E}}{\partial x} + \frac{\partial \mathbf{F}}{\partial y} + \frac{\partial \mathbf{G}}{\partial z} = 0, \quad (1)$$

With vectors \mathbf{W} , \mathbf{E} , \mathbf{F} , and \mathbf{G} given by:

$$\mathbf{W} = \begin{bmatrix} w_1 \\ w_2 \\ w_3 \\ w_4 \\ w_5 \end{bmatrix} = \begin{bmatrix} \rho \\ \rho u \\ \rho v \\ \rho w \\ E \end{bmatrix}, \quad \mathbf{E} = \begin{bmatrix} \rho u \\ \rho u^2 + P \\ \rho u v \\ \rho u w \\ (E + P)u \end{bmatrix}, \quad (2)$$

$$\mathbf{F} = \begin{bmatrix} \rho v \\ \rho u v \\ \rho v^2 + P \\ \rho u w \\ (E + P)v \end{bmatrix}, \quad \mathbf{G} = \begin{bmatrix} \rho w \\ \rho u w \\ \rho v w \\ \rho w^2 + P \\ (E + P)w \end{bmatrix}.$$

Where, u , v , and w are the Cartesian velocity components, E is the total energy per unit volume, P is the pressure, and $(w_1, w_2, w_3, w_4, w_5)$ are the components of the unknown vector \mathbf{W} .

The first row of the vector equation (i.e. Equation (1)), vectors \mathbf{W} , \mathbf{E} , \mathbf{F} , and \mathbf{G} correspond to the continuity equation, the second, third, and fourth rows are the momentum equation in x , y , and z direction and the fifth row is the energy equation. The vector \mathbf{W} contains the time dependent variables. If this vector is neglected, the remaining terms would be the steady state Euler equations. The mathematical character of the steady Euler equations in subsonic flows is elliptic while at supersonic flows their character changes to that of hyperbolic. However, by keeping the vector \mathbf{W} , the existing unsteady Euler equations in all of the flow regimes including subsonic, transonic, and supersonic form a hyperbolic system of partial differential equations. The unsteady Euler equations can then be solved by a time-marching method to arrive at their steady state solution.

To complete the above equations, the ideal gas law equations can be used in the following manner.

$$p = \rho R T, \quad e = c_v T, \quad \gamma = c_p / c_v \quad (3)$$

$$E = \rho e + \frac{1}{2} \rho (u^2 + v^2 + w^2). \quad (4)$$

Where, c_p is the specific heat at constant pressure, c_v is the specific heat at constant volume, R is the universal gas constant, and γ is the ratio of specific heats. For air, $\gamma = 1.4$, and $R = 287$ (m²/s²K).

The state equations as a result of the non-dimensional parameters would become:

$$p = \rho T, \quad T = (\gamma - 1)e, \quad P = (\gamma - 1)\rho e, \quad (5)$$

$$E = \frac{P}{(\gamma - 1)} + \frac{1}{2} \rho (u^2 + v^2 + w^2). \quad (6)$$

The next step in solving the three-dimensional Euler equation requires the spatial discretization of the governing flow equations. The discretized equations are then marched through time to reach a steady state solution. The procedures and formulation of these steps are discussed in the following sections.

4 Numerical Discretization

Having derived the governing flow equations the next stage is the development of a solution procedure associated with the numerical discretization of these equations. In the present work, the Euler equations are first discretized in space. Subsequently, in a second step, they will be integrated in time to a steady-state solution (cf. Jameson et al [6]). This approach, the so-called "method of lines", leads to a system of non-linear ordinary differential equations. Thus, a finite-volume spatial discretization is used and the computational domain is divided into a finite number of non-overlapping sub-domains or control-volumes.

4.1 Finite-Volume Spatial Discretization

Finite-volume methods have become very popular during the last few decades, mainly because they present some advantages of both the finite-difference and the finite-element schemes (Hirsch [2]). In particular, they are very suitable for equations in conservation form and can be applied to the equations directly in the physical space without the need to transform them into a computational space. The advantage is an increase in flexibility of the method since all of the problems associated with the evaluation of the Jacobians of the transformation matrix are removed.

The finite-volume method applied to the governing equations can be obtained by integrating Equations (1) over the domain of interest Ω .

$$\frac{\partial}{\partial t} \int_{\Omega} \mathbf{W} d\Omega + \int_{\Omega} (\nabla \cdot \mathbf{F}) d\Omega = 0, \quad (7)$$

where ∇ is the divergence operator in Cartesian coordinates. By applying the Gauss theorem to the second term of Equation (7), the system becomes:

$$\frac{\partial}{\partial t} \int_{\Omega} \mathbf{W} d\Omega + \oint_{\partial\Omega} \mathbf{F} \cdot \mathbf{n} ds = 0. \quad (8)$$

Where $\partial\Omega$ is the boundary of the domain Ω and \mathbf{n} is the unit outward normal vector. The main property of the above form is that the evaluation in time of the conserved quantities \mathbf{W} depends only on the distribution of the flux \mathbf{F} on the boundary $\partial\Omega$. Therefore, the problem of determining \mathbf{W} over Ω is reduced to the determination of the flux on the contour of the domain of interest.

In the finite-volume method, the computational domain is divided in several sub-domains or control volumes and the conservation laws (1) are applied to each of the resulting sub-domains. For each generic control volume K of volume Ω_K Equation (8) can be re-written as:

$$\frac{\partial}{\partial t} \int_{\Omega_K} \mathbf{W} d\Omega + \oint_{\partial\Omega_K} \mathbf{F} \cdot \mathbf{n} ds = 0. \quad (9)$$

This becomes a system of integral-differential equations in time.

The finite-volume method allows certain choices of control-volume to be used as the computational grid. In the present work, the cell-centered finite volume approach is used and, therefore, from now onwards, the terms "cell" and "control-volume" will refer to the grid cells only. As a consequence, the unknown variables \mathbf{W} are associated with the centers of the cells (See Fig. 3).

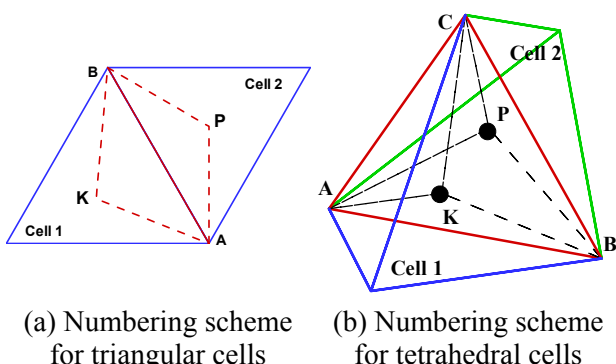


Fig. 3 Main and auxiliary computational cells or control-volumes with cell centers \mathbf{K} and \mathbf{P} , for neighboring: (a) triangular and (b) tetrahedral cells

In order to use Equation (9) for the components of \mathbf{W} , a further assumption has to be introduced. In fact, because the distribution of \mathbf{W} over the cell is not known, the first integral in Equation (9) cannot be evaluated explicitly. However, by applying the mean-value theorem to the control volume Ω_K , expression (10) for the average value $\bar{\mathbf{W}}$ is obtained.

$$\bar{\mathbf{W}} = \frac{1}{\Omega} \int_{\Omega} \mathbf{W} d\Omega = 0. \quad (10)$$

The Equation (9) can now be written as:

$$\frac{\partial \Omega_K \bar{\mathbf{W}}_K}{\partial t} + \oint_{\partial\Omega_K} \mathbf{F} \cdot \mathbf{n} ds = 0. \quad (11)$$

If the cell volume is constant in time, the above equation can be divided by the control volume Ω_K , which results in:

$$\frac{\partial \bar{\mathbf{W}}_K}{\partial t} + \frac{1}{\Omega_K} \oint_{\partial\Omega_K} \mathbf{F} \cdot \mathbf{n} ds = 0. \quad (12)$$

In this manner, Equation (12) contains the cell-averaged values of the unknown conserved variables. This indicates that only the averaged values of \mathbf{W} and not the local values are known after the solution process.

An important consequence of the mean-value theorem is that if the values of the conserved variables \mathbf{W} are assumed to be constant or vary linearly over the control volume Ω , the value at the center of the cell \mathbf{W}_C , is equal to the mean-value $\bar{\mathbf{W}}$:

$$\mathbf{W}_C = \bar{\mathbf{W}} = \frac{1}{\Omega} \int_{\Omega} \mathbf{W} d\Omega = 0. \quad (13)$$

The coordinates of the cell centroids for a three-dimensional computational cell, such as the one shown in Fig. 3(b), are:

$$\begin{aligned} x_C &= \frac{1}{\Omega} \int_{\Omega} x d\Omega, \\ y_C &= \frac{1}{\Omega} \int_{\Omega} y d\Omega, \\ z_C &= \frac{1}{\Omega} \int_{\Omega} z d\Omega. \end{aligned} \quad (14)$$

Considering the flux vectors for a three-dimensional case in terms of the Cartesian unit vectors $\mathbf{F} = \mathbf{F}_x i + \mathbf{F}_y j + \mathbf{F}_z k$, where ($\mathbf{F}_x = \mathbf{E}$, $\mathbf{F}_y = \mathbf{F}$, $\mathbf{F}_z = \mathbf{G}$), equations (1) and (14) are combined and for a typical control-volume K fixed in time can be approximated by:

$$\frac{\partial \bar{\mathbf{W}}_K}{\partial t} + \frac{1}{\Omega_K} \sum_{i=1}^{K_{faces}} (\mathbf{E}_i \Delta S x_i + \mathbf{F}_i \Delta S y_i + \mathbf{G}_i \Delta S z_i) = 0. \quad (15)$$

The summation is over the n-faces forming the cell-K, \mathbf{E}_i , \mathbf{F}_i , and \mathbf{G}_i are the Cartesian components of the flux at the ith face, and $(\Delta S x_i, \Delta S y_i, \Delta S z_i)$ are components of the area outward normal vector (n ds) or ΔS_i associated with face-i. Depending on the geometry of the face area, in this case a triangular face of a tetrahedron, the components of the area ΔS_i are defined by its three forming vertices (A, B, and C). These vertices are detailed in Fig. 3(b) for a triangular face-i (shown in red) and are defined as follows.

$$\Delta S x = \frac{1}{2} [(Y_B - Y_A)(Z_C - Z_A) - (Y_C - Y_A)(Z_B - Z_A)] \quad (16)$$

$$\Delta S y = -\frac{1}{2} [(X_B - X_A)(Z_C - Z_A) - (X_C - X_A)(Z_B - Z_A)]$$

$$\Delta S z = \frac{1}{2} [(X_B - X_A)(Y_C - Y_A) - (X_C - X_A)(Y_B - Y_A)]$$

The flux components at the i^{th} face can be evaluated either using the values of the surrounding cell centers (i.e. K and P in Fig. 3) or by using the values of the conserved variables. In the present work, the convective fluxes at the cell face-i are evaluated by using the flow variables on the cell face itself.

$$\mathbf{E}_i(\mathbf{W}) = \mathbf{E}(\mathbf{W}_i),$$

$$\mathbf{F}_i(\mathbf{W}) = \mathbf{F}(\mathbf{W}_i), \quad (17)$$

$$\mathbf{G}_i(\mathbf{W}) = \mathbf{G}(\mathbf{W}_i).$$

Where: \mathbf{W}_i is the value of the conserved variable at the i^{th} face. The simplest approach to calculate the dependent variables on the cell face is to average the values of the two cell-centers (see Fig. 3):

$$\mathbf{W}_i = \frac{\mathbf{W}_K + \mathbf{W}_P}{2}. \quad (18)$$

Equations (17) and (18) lead to a second-order central difference formulation on an orthogonal uniform Cartesian grid, which is satisfactory for the mean-flow equations. However, for non-orthogonal shapes, they require especial considerations which are detailed in the following section.

4.2 Central Difference Scheme

If the finite volume scheme of Equation (17) is used to evaluate the convective fluxes as in Equation (18), the resulting scheme becomes identically equal to the standard three-point central difference scheme in three dimensions. Thus, the present finite-volume scheme is second order accurate, at least for orthogonal meshes.

However, finite-volume schemes depart from the standard finite-difference schemes when applied to curvilinear reference systems. This is due to the fact that the finite-volume schemes do not involve any coordinate transformation.

The finite-volume scheme described in the previous section is essentially a central scheme as pointed out here. Therefore, the scheme is non-dissipative and when applied to convection problems such as the Euler equations, spurious oscillations are not damped. This can affect the quality of the numerical solution as well as the convergence rate. To overcome this problem, artificial dissipation terms may be added to the finite-volume equations as described in the following section.

5 Numerical Dissipation

Second-order central discretization schemes are essentially non-dissipative. Hence, when applied to the convective terms of the mean-flow equations [i.e. Equation (15)], they can generate undamped oscillations that affect the quality of the solution and can result in a deterioration of the convergence. Oscillations are generally produced by the odd-even point decoupling which is present in central schemes. Subsequently the spatial errors change the sign at consecutive points producing high-frequency

oscillations that will not be damped as the steady-state solution is approached. Another type of oscillation can be triggered by discontinuities in the solution (i.e. shock waves) which can be rather intense and propagate rapidly throughout the flow domain.

In order to remove these types of instabilities, one can employ an upwind scheme, which is only first-order accurate. Second-order spatial accuracy can be achieved by introducing more upwind points in the difference formulation. This however leads to the generation of oscillations around discontinuities similar to those encountered with central schemes. Therefore, extensive research has been carried out to achieve the goal of oscillation-free, and higher-order upwind schemes capable of predicting shock waves as well as contact discontinuities accurately.

A variety of methods have been developed that are based on Total Variation Diminishing (TVD) properties. These methods are now well defined for one-dimensional flows. However, the complexity of the method increases as multidimensional flows are considered. In general, multi-dimensional problems are approximated by a series of one-dimensional approaches. This approach is suitable for use with structured grids, but leads to some difficulties when unstructured grids are considered.

An alternative, more straightforward, approach to elimination of the spurious oscillations is to retain the central discretization for the convective fluxes, and add just enough numerical dissipation where needed. This method basically introduces numerical dissipation terms into the Euler solution of inviscid flows, to control numerical instabilities and to enable the clean capture of shock waves.

A blending of second and fourth differences of the flow variables \mathbf{W}_K has been introduced and added to the system of mean flow equations in such a way that the conservation form of the equations is preserved:

$$\frac{d\mathbf{W}_K}{dt} = -(\mathbf{F}_K - \mathbf{D}_K). \quad (19)$$

Where \mathbf{F}_K is the discrete flux vector and \mathbf{D}_K is the dissipation function. The idea is to add third order dissipation terms throughout the domain, to provide a base level of dissipation sufficient to prevent non-linear oscillations, apart from near shock waves where it may cause instabilities. In order to capture shock waves, additional first-order dissipation terms are added locally by a sensor designed to detect discontinuities. The dissipation

function \mathbf{D}_K can now be written for unstructured grids (cf. Jameson and Mavriplis [8]) as:

$$\mathbf{D}_K = \sum_{i=1}^{K_{faces}} d_i^{(2)} + d_i^{(4)}. \quad (20)$$

with:

$$d_i^{(2)} = \alpha_i \varepsilon_i^{(2)} (\mathbf{W}_P - \mathbf{W}_K), \quad (21)$$

$$d_i^{(4)} = -\alpha_i \varepsilon_i^{(4)} (\nabla^2 \mathbf{W}_P - \nabla^2 \mathbf{W}_K). \quad (22)$$

where, ∇^2 is the undivided Laplacian operator on a three-dimensional tetrahedral grid:

$$\nabla^2 \mathbf{W}_K = \sum_{i=1}^{K_{faces}} (\mathbf{W}_P - \mathbf{W}_K)_i. \quad (23)$$

and α_i is an appropriate scaling factor related to the maximum eigenvalues of the convective Jacobian matrices on the i^{th} face.

$$\alpha_i = \left| u_i \Delta Sx_i + v_i \Delta Sy_i + w_i \Delta Sz_i \right| + c_i \sqrt{\Delta Sx_i^2 + \Delta Sy_i^2 + \Delta Sz_i^2}. \quad (24)$$

where u , v , and w are components of the velocity vector at the face- i , c_i is the local speed of sound $c_i = \sqrt{\gamma P_i / \rho_i}$, and $(\Delta Sx_i, \Delta Sy_i, \Delta Sz_i)$ are components of the area outward normal associated with face- i which were expressed by relations (16) for a triangular face. The adaptive coefficients $\varepsilon_i^{(2)}$ and $\varepsilon_i^{(4)}$ are defined as follows:

$$\varepsilon_i^{(2)} = k^{(2)} v_i, \quad (25)$$

$$\varepsilon_i^{(4)} = \max [0, (k^{(4)} - \varepsilon_i^{(2)})]. \quad (26)$$

Where $k^{(2)}$ and $k^{(4)}$ are empirically-chosen constants, which usually take values in the ranges $(0.5 < k^{(2)} < 1)$ and $(1/256 < k^{(4)} < 1/32)$, and v_i is a shock sensor.

The construction of the shock sensor is a crucial matter since it has an effective control on the level of dissipation introduced in the flow domain. The original structured grid based sensor was devised in

the form of a non-dimensional second difference of pressure which takes into account the contribution of dissipation along each direction individually. However, the unstructured equivalent of this formulation proposed by Jameson et al [5] switches on or off in all directions at the same time:

$$\nu_K = \frac{\left| \sum_{i=1}^{K_{faces}} (P_p - P_k)_i \right|}{\left| \sum_{i=1}^{K_{faces}} (P_p + P_k)_i \right|}. \quad (27)$$

As investigated by Stolcis and Johnston [7], this isotropic behavior not only increases the level of artificial dissipation in the regions where the solution is smooth, but results in an insufficient level of dissipation in the proximity of discontinuities. In order to remove this problem, the single shock sensor for each cell, is replaced by a non-isotropic sensor for each face:

$$\nu_i = \left(\frac{|(P_p - P_k)|}{|(P_p + P_k)|} \right)_i. \quad (28)$$

The above sensor has worked well with several Euler and Navier-Stokes problems as reported by Stolcis and Johnston [7] when employed with the edges of two-dimensional unstructured triangular grid cells. In smooth regions of the flow, where the pressure gradients are small, ν_i is also small ($\nu_i \ll 1$), therefore, $\varepsilon_i^{(2)}$ and $d_i^{(2)}$ are negligible while $\varepsilon_i^{(4)}$ is of order one forming the main contribution to \mathbf{D}_k . In the neighborhood of a shock wave, ν_i is of order one where the fourth difference term is switched off through the relation between $\varepsilon_i^{(2)}$ and $\varepsilon_i^{(4)}$, which is given by Equation (26).

6 Time Discretization

Once the spatial discretization is performed, as described in the previous section, the governing mean-flow equations (i.e. the Euler equations) become a system of ordinary differential equations in time:

$$\frac{d\mathbf{W}_k}{dt} = \mathbf{R}_k. \quad (29)$$

Where, \mathbf{R}_k is the residual or deviation from the steady-state solution for each cell k , and can be written as:

$$\mathbf{R}_k = -(\mathbf{F}_k - \mathbf{D}_k), \quad (30)$$

and the right-hand side terms are as described in equation (19).

The methods available for solving a system of ordinary differential equations can be classified into two different categories: implicit and explicit methods. Explicit methods evaluate the residual \mathbf{R}_k using only values obtained from the previous iteration step, whilst implicit methods use also values at current iteration step. Several implicit methods are available and are reviewed by Hirsch [2]. These methods are actually suitable for steady-state calculations because they do not have restrictions on the maximum allowable time step, and thus require less iterations to reach the final solution.

On the other hand, explicit methods can be easily implemented on unstructured grids, require less memory, and can be efficiently adapted for use with parallel computers. It should be noted however that explicit methods require more iterations in order to reach the steady-state solution since the size of their maximum allowable time-step is limited due to stability constraints. Therefore, techniques such as local time stepping, residual smoothing, and multi-grid can be employed to accelerate convergence (Jameson [5]). In the present work an explicit time-marching scheme is used whose details are given in the following section.

6.1 Explicit Time marching Scheme

Time integration of equation (29) is performed using an explicit multi-stage scheme. The standard form of an M-stage Runge-Kutta scheme can be written as:

$$\begin{cases} \mathbf{W}^{(0)} = \mathbf{W}^n \\ \dots \\ \mathbf{W}^{(m)} = \mathbf{W}^{(0)} + \alpha_m \Delta t \mathbf{R}^{(m-1)} \\ \dots \\ \mathbf{W}^{(n+1)} = \mathbf{W}^M \end{cases} \quad (31)$$

Where n is the current time level, (n+1) is the new time level, (m) is the intermediate stage, and M is the total number of stages. A 4-stage scheme is adopted here because of its stability properties, with coefficients of:

$$\alpha_1 = \frac{1}{4}, \quad \alpha_2 = \frac{1}{3}, \quad \alpha_3 = \frac{1}{2}, \quad \alpha_4 = 1 \quad (32)$$

However, in order to minimize the computational time, the expensive calculations of the dissipation term D is only performed once, at the first stage (0). The values at all remaining stages are frozen; thus the residual in Equation (30) at each intermediate stage (m) is given by:

$$\mathbf{R}_K^{(m)} = -(\mathbf{F}_K^{(m)} - \mathbf{D}_K^{(0)}). \quad (33)$$

The maximum CFL number for the above scheme is about $2\sqrt{2}$ if applied to the Euler equations cf. Jameson [5]).

7 Initial and Boundary Conditions

The next and final task before start of computations is to define the appropriate initial and boundary conditions of the flow domain. These conditions are given in the following sections.

7.1 Initial Conditions

As far as the numerical integration scheme is concerned, the most important consequence is that the steady-state solution becomes independent of the initial conditions employed. The initial conditions at time ($t=0$), applied in the present method, consist of setting all the quantities equal to their free stream values. This corresponds to a sudden insertion of the solid body (i.e. cylinder, wing, etc.) in an undisturbed flow with free stream conditions everywhere.

The non-dimensional free stream values are expressed in terms of the free stream density ρ_∞ , Pressure P_∞ , Mach number M_∞ , incidence angle α , and side slip or yaw angle β . With the yaw angle β set to zero and having a non-dimensional value of 1 for the free stream density and pressure, the initial conditions become:

$$\begin{aligned} P_\circ &= P_\infty = 1, & \rho_\circ &= \rho_\infty = 1, \\ u_\circ &= M_\infty \sqrt{\gamma} \cos \alpha, & v_\circ &= 0, \\ w_\circ &= M_\infty \sqrt{\gamma} \sin \alpha. \end{aligned} \quad (34)$$

Where, the subscript \circ denotes initial conditions.

For the solution of most problems in compressible flow, the continuity, momentum, and energy equations are sufficient. However, for an inviscid adiabatic flow, it can be shown that the entropy of a moving fluid element is constant.

$$ds/dt = 0, \quad (35)$$

$$s = \text{constant}.$$

If the flow is steady, the entropy (s) is constant along a streamline in an adiabatic inviscid flow. Moreover, if the flow originates in a constant entropy reservoir, such as the free stream far ahead of a moving body, each streamline has the same value of entropy, and hence Equation (35) holds throughout the complete flow field. For isentropic flows, Equation (35) is frequently convenient, and may be used to substitute for either the energy or momentum equations. Therefore, the variation of energy on the surface of solid geometry can be expressed by the variation of entropy.

$$s = (P/\rho^\gamma) - s_\circ. \quad (36)$$

The initial value for the entropy is calculated by applying the initial conditions as shown below.

$$s_\circ = (P_\circ/\rho_\circ^\gamma) = 1. \quad (37)$$

It should be noted that Equation (35) is valid for both steady and unsteady flows and has some advantages, when shock waves have to be investigated.

7.2 Solid-wall Boundary Conditions

The inviscid wall boundary condition imposes flow tangency at the surface boundary (wall surface). The component of the velocity normal to the wall boundary is set to zero.

$$u_\omega = v_\omega = w_\omega = 0. \quad (38)$$

A further condition for the pressure is obtained by using a simple zero-th order extrapolation and the pressure at the wall is set equal to the pressure at the center of the near wall cell:

$$\left(\frac{\partial P}{\partial y_n} \right)_\omega = 0 . \quad (39)$$

Where the subscript ω , indicates conditions at the wall and y_n is the surface normal distance.

7.3 Outer Boundary Conditions

On the outer boundary, it is not possible to define the boundary conditions in a unique manner. Since the computations are inviscid, the characteristic based boundary conditions developed for inviscid flows can be applied. The conditions employed are based on one-dimensional Riemann-invariant theory for the flow normal to the boundary (cf. Jameson and Baker [6]). The Riemann invariants are given as:

$$R^+ = u_n + \frac{2c}{\gamma - 1}, \quad R^- = u_n - \frac{2c}{\gamma - 1}. \quad (40)$$

Where u_n is the mean-velocity component normal to the boundary surface (the outer-boundary triangular face in this case) and c is the speed of sound. At each point on the outer boundary the values are either extrapolated from the inner points (ext) if the flow is outgoing, or set equal to the free stream values (∞) if the flow is incoming. Therefore, R^+ and R^- can be re-written as follows:

$$R_{ext}^+ = u_{n_{ext}} + \frac{2c_{ext}}{\gamma - 1}, \quad R_\infty^- = u_{n_\infty} - \frac{2c_\infty}{\gamma - 1}. \quad (41)$$

For subsonic inflow and outflow, the normal mean-velocity component and the speed of sound are given by the Riemann invariants as:

$$u_n = \frac{1}{2}(R_{ext}^+ + R_\infty^-), \quad c = \frac{\gamma - 1}{4}(R_{ext}^+ - R_\infty^-). \quad (42)$$

If the flow is outgoing, two additional conditions are required concerning entropy and tangential velocity, which are extrapolated from the interior. These quantities are set to their free stream values if the flow is incoming. The pressure is determined using the definition of the speed of sound

($c = \sqrt{\gamma P / \rho}$). For supersonic outflow and inflow, all of the variables are extrapolated from the interior or set to their free stream values, respectively.

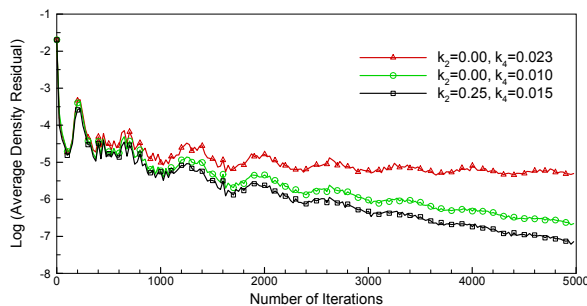
8 Computational Results

The mathematical formulation of the Euler equations and the finite-volume solution techniques along with the initial and boundary conditions, described in the previous sections, have been implemented in computer codes. These codes are written in the FORTRAN language and work in parallel with the two- and three-dimensional unstructured grid generators. As discussed in the previous Section, the Euler flow solvers employ finite-volume spatial discretization and an explicit multi-stage Runge-Kutta time discretization. The unsteady Euler equations are marched in time to reach a steady state solution.

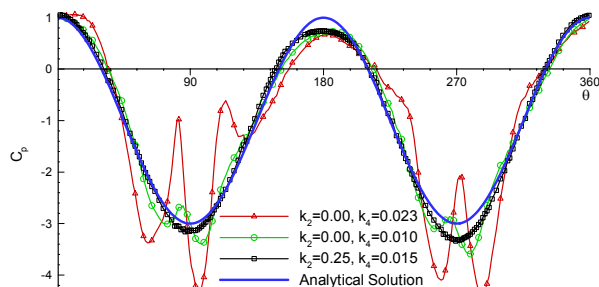
The objective of this paper is to present the flow solutions, with emphasis on the two numerical dissipation coefficients, $k^{(2)}$ and $k^{(4)}$, as a result of employing the Euler flow solvers with unstructured grids. The flow solvers give the solution results over the entire flow domain. Here, the surface solutions, which give the required flow characteristics, are presented for each computational case.

The first and second case involved the flow over a 2-dimensional circular cylinder at free stream Mach numbers of 0.3 and 0.45, while the third and forth computational cases describe 3-dimensional flow over a circular cylinder attached to a plane of symmetry at free stream Mach numbers of 0.3 and 0.8. These cases were selected to demonstrate the effect of varying the values of artificial dissipation terms.

The computational unstructured grid shown in Fig. 1(b) was employed for the first case with free-stream Mach number of 0.3. The resulting flow solutions with various dissipation coefficients, $k^{(2)}$ and $k^{(4)}$, are given in Fig. 4. The convergence history for three different solutions up to 5000 iterations is shown in Fig. 4(a). The pressure coefficients for these solutions are plotted over the cylinder section and are shown in Fig. 4(b), where, these C_p values are compared with an inviscid analytical solution. The optimal values for the dissipation coefficients, $k^{(2)}$ and $k^{(4)}$, are found to be 0.25 and 0.015 respectively. The pressure and Mach number contours for the solution with these optimal values are plotted over the cylinder surface and are shown in Fig.s 4(c) and 4(d).



(a) Convergence history for flow solutions with various dissipation coefficients, $k^{(2)}$ and $k^{(4)}$



(b) Pressure coefficient plots for various dissipation coefficients, $k^{(2)}$ and $k^{(4)}$

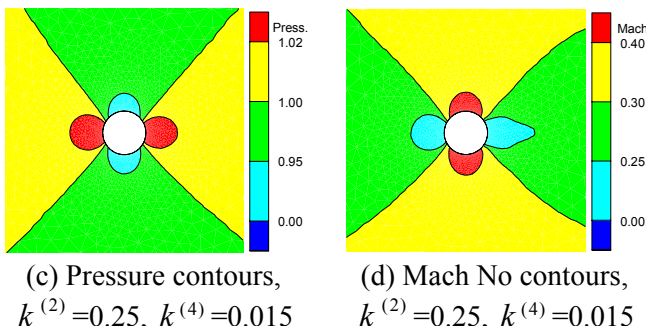
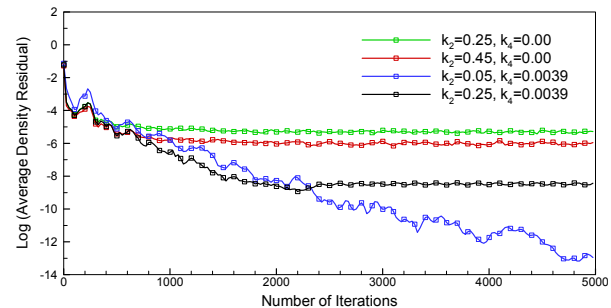


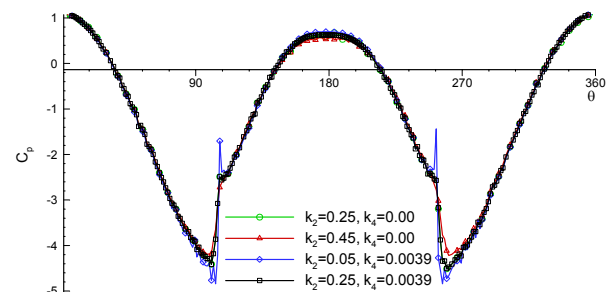
Fig. 4 First case, Two-dimensional flow solution results around a circular cylinder, $M_\infty = 0.3$

The same computational grid shown in Fig. 1(b) was employed for the second case with a free-stream Mach number of 0.45. This was done to reach transonic conditions. The resulting flow solutions with various dissipation coefficients, $k^{(2)}$ and $k^{(4)}$, are given in Fig. 5. History of the solution convergence is shown in Fig. 5(a), where four different solutions are presented. The pressure coefficients for these four solutions are plotted over the cylinder section and are shown in Fig. 5(b). It is clear that two strong shocks are present over the cylinder surface for all the runs in this test case. The shock waves are best captured with 0.25 and 0.0039

for the set of dissipation coefficients. Figs. 5(c) and 5(d) show the pressure and Mach number contours for the solution run with the $k^{(2)}$ and $k^{(4)}$, values of 0.25 and 0.0039.



(a) Convergence history for flow solutions with various dissipation coefficients, $k^{(2)}$ and $k^{(4)}$



(b) Pressure coefficient plots for various dissipation coefficients, $k^{(2)}$ and $k^{(4)}$

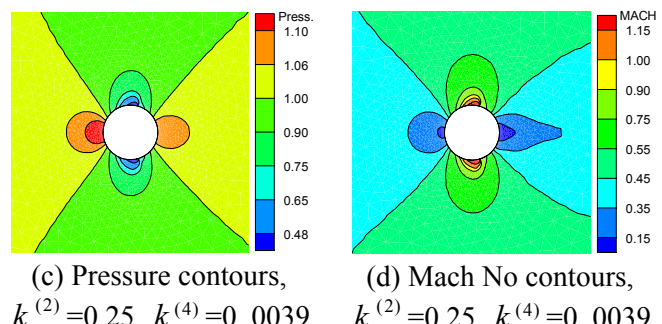


Fig. 5 Second case, Two-dimensional flow solution results around a circular cylinder. $M_\infty = 0.45$

To show consistency with higher order spatial discretization, sample solutions are presented in three-dimensions. The computational grid for the circular cylinder of diameter 1 and length 4 attached to a plane of symmetry shown in Fig. 2 was employed for the three dimensional cases. Euler flow solutions were obtained at free-stream Mach number of 0.3 and 0.8.

At a free-stream Mach number of 0.3, solutions were obtained for different values of the 1st order dissipation coefficient $k^{(2)}$, and are shown in Fig. 6. It is shown that by reducing the 1st order adjustable dissipation coefficient, $k^{(2)}$, coefficient of pressure values over the entire span of the cylinder move closer to their analytical inviscid solution.

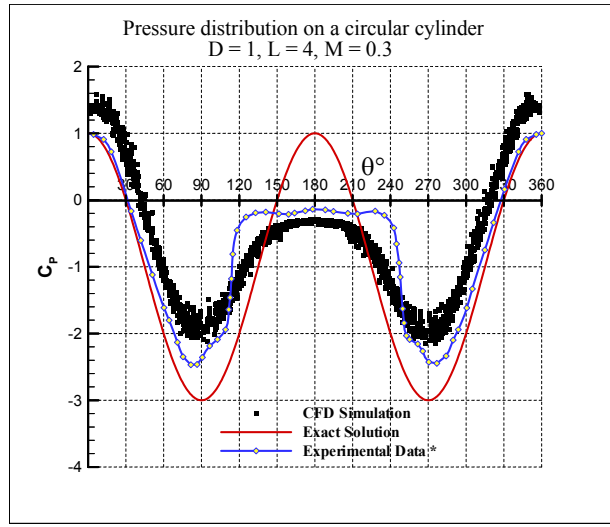
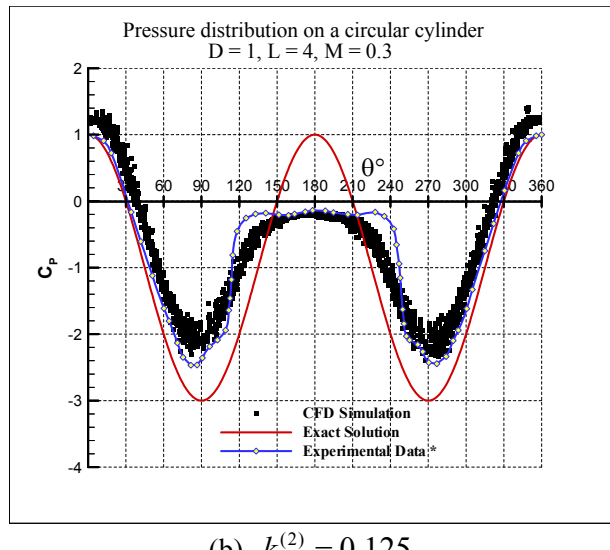
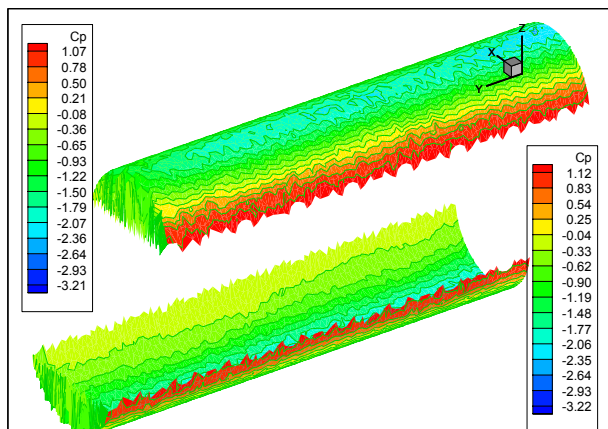
(a) $k^{(2)} = 0.25$ (b) $k^{(2)} = 0.125$

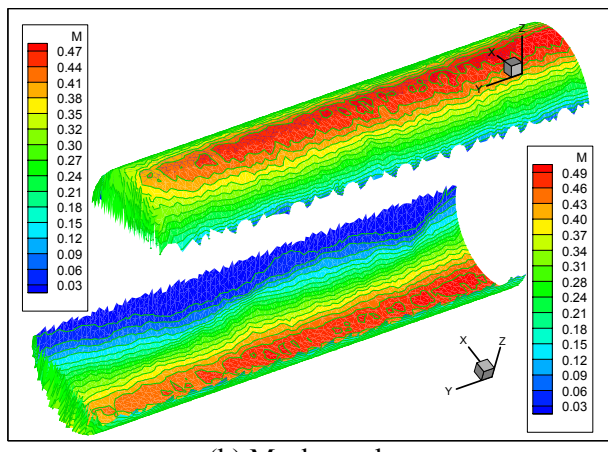
Fig. 6 Pressure distribution on a circular cylinder with various 1st order dissipation $k^{(2)}$,
Cylinder: $D = 1$, $L = 4$, $\alpha = 0^\circ$, $M_\infty = 0.3$,
* Experimental data, Schlichting [9] at $Re=6.7 \times 10^5$

Fig. 7 shows the pressure, Mach number, and entropy contours on the upper and lower surfaces of the circular cylinder for the solution at $M_\infty = 0.3$

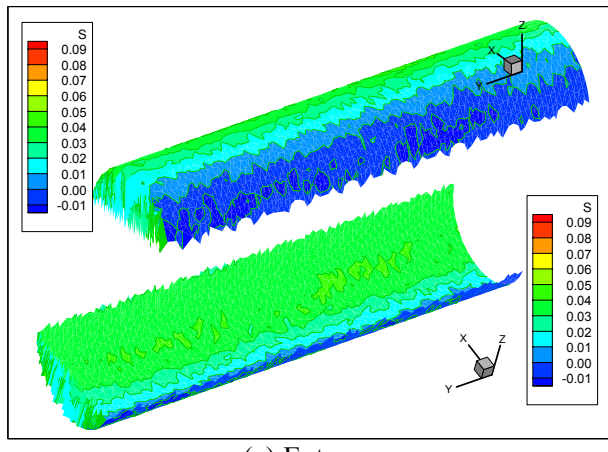
with $k^{(2)} = 0.125$. It should be noted that the direction of the free-stream flow in all of the computational cases is from negative x-axis towards the positive x-axis. In other words, the front stagnation point occurs at location $\theta = 0^\circ$ on the cylinder.



(a) Pressure coefficients



(b) Mach number



(c) Entropy

Fig. 7 Pressure, Mach number, and entropy contours on the upper and lower surfaces of the circular cylinder, $M_\infty = 0.3$, and $k^{(2)} = 0.125$

To show the effect of adjustable dissipation coefficients for a more realistic transonic flow, solutions with a free stream Mach number of 0.8 are obtained with the 1st order dissipation $k^{(2)}$ values of 0.25 and 0.125 as the forth and last case. Coefficients of pressure points along the span of the cylinder are compared with an analytical inviscid solution in Fig. 8. Again, it can be seen that by reducing the amount of the 1st order dissipation $k^{(2)}$, coefficient of pressure points along the span of move closer to the analytical inviscid curve.

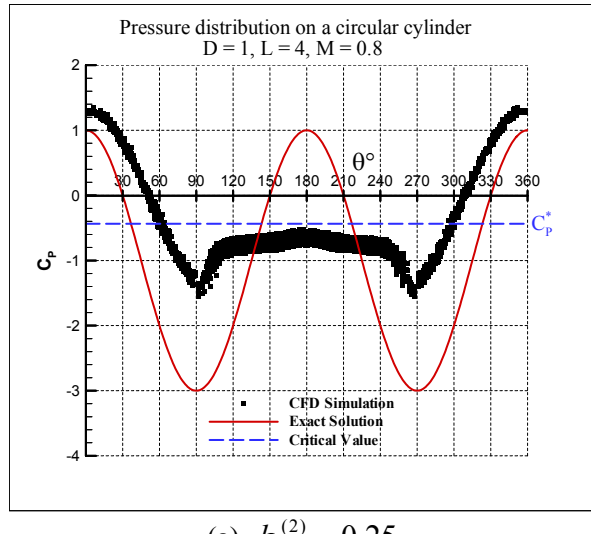
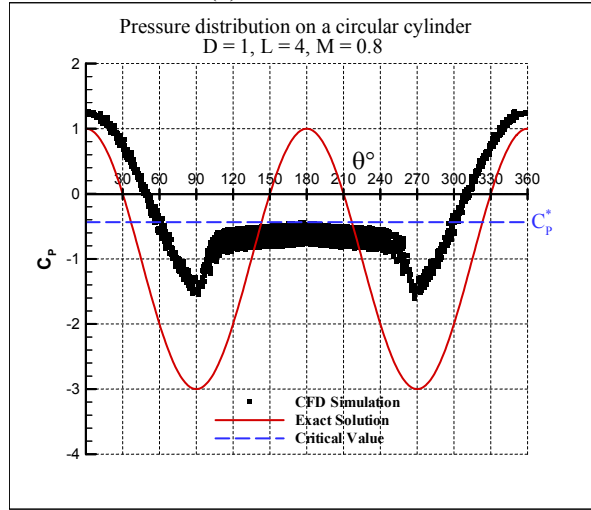
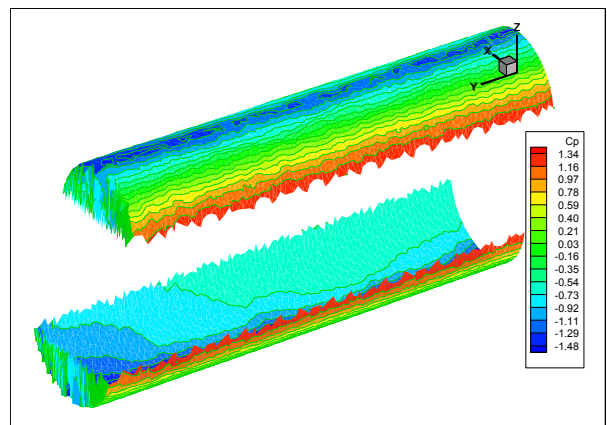
(a) $k^{(2)} = 0.25$ (b) $k^{(2)} = 0.125$

Fig. 8 Pressure distribution on a circular cylinder with various 1st order dissipation $k^{(2)}$,
Cylinder: D = 1, L = 4, $\alpha = 0^\circ$, $M_\infty = 0.8$,
* Experimental data, Schlichting [9] at $Re = 6.7 \times 10^5$

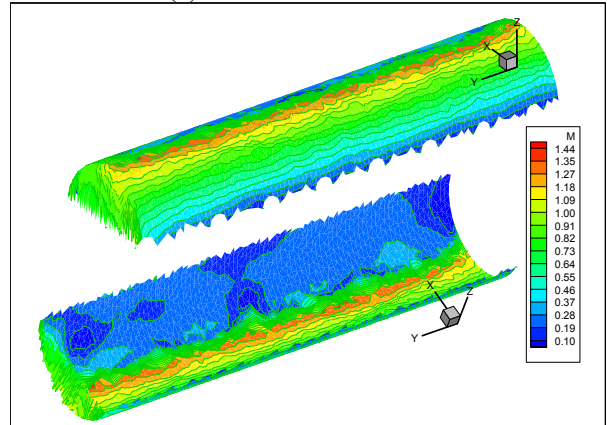
The pressure, Mach number, and entropy contours on the upper and lower surfaces of the circular cylinder for this case are displayed in Fig. 9. The pressure contours, in this case, show a strong

change at the leading edge. Since the flow started with a free stream Mach number of 0.8, a strong shock is present on the cylinder shoulder and is shown in Fig. 9 (c).

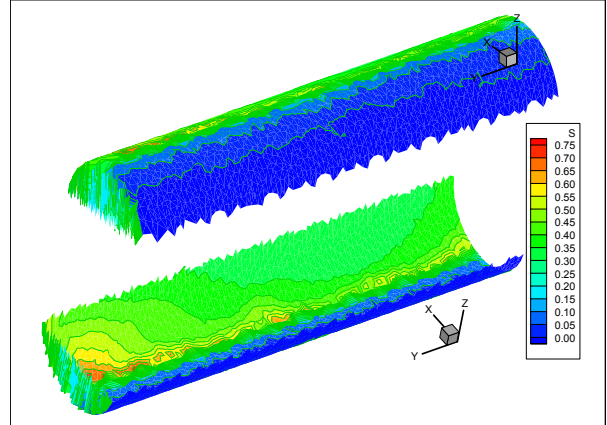
The entropy contours, shown in Fig. 9(d), show a rapid change at the cylinder shoulder and remain constant elsewhere. Again, this is due to the presence of shock on the cylinder shoulder and inviscid behaviour in other regions.



(a) Pressure coefficients



(b) Mach number



(c) Entropy

Fig. 9 Pressure coefficient, Mach number, and entropy contours on the upper and lower surfaces of the circular cylinder, $M_\infty = 0.8$, and $k^{(2)} = 0.125$

9 Conclusion

The discretized Euler flow equations are essentially non-dissipative. Hence, convective terms of the flow equations can generate spurious oscillations that can affect the quality of the solution and can result in a deterioration of the convergence. A small amount of numerical dissipation is added to damp the oscillations enabling the flow solution to reach its steady state conditions. Thus, by reducing the amount of numerical dissipation (1st order dissipation in this case) that is needed to control the spurious oscillations, instabilities will occur. The objective of this paper is to illustrate the effect that the amount of added dissipation has on the quality of the flow solution. For this objective, Euler flow solutions of varying first- and third-order dissipation coefficients have been investigated.

The first example considers a subsonic flow solution with a free-stream Mach number of 0.3 over a circular cylinder. Initially, first-order dissipation coefficients were turned off and an arbitrary small value was selected for the third-order dissipation coefficient. This caused instabilities in the flow solution and is clearly shown in Fig. 4(b). Although at this Mach number no shock is present, disturbances are caused by the strong change in the pressure at the leading edge stagnation point. The small amount of the third-order dissipation coefficient, $k^{(4)}$, was sufficient enough to enable the flow solution to converge. This third-order dissipation coefficient was reduced empirically to obtain an optimal value for $k^{(4)}$ in the absence of first order coefficient. Since the third order dissipation coefficient is present throughout the entire flow domain, it is essential to keep this coefficient at a minimal value to avoid over damping the regions of high pressure gradients. Finally, to properly control the oscillations in these regions, first-order dissipation coefficients were turned on and the solutions are shown to match their analytical values.

To demonstrate the above procedure for a more realistic condition expected of inviscid flows, characterized by shock waves, similar analysis were performed on the cylinder with a free stream Mack number of 0.45. In this case, values of 0.25 and 0.0039 were found to be the optimal values for the set of dissipation coefficients, $k^{(2)}$ and $k^{(4)}$. This can be seen in Fig. 5(b), where pressure coefficient plots of different test runs are compared.

The third case presented here involved the solution of Euler equations on a three dimensional cylinder section attached to a plane of symmetry. This geometry which was shown in Fig. 2, was

selected for analogy with the two dimensional cases. Initial conditions for this case included the free stream Mach number of 0.3 at zero attack angle, and varying values of the dissipation coefficients.

The forth and last computational case presented here aims to demonstrate the extent of these studies to transonic flow conditions. For this reason and analogy with the two-dimensional cases presented earlier, the sample tetrahedral grid generated for a circular cylinder was used again. Several Euler flow solutions were obtained by employing this unstructured tetrahedral grid. Two sample runs at transonic Mach number of 0.8 were presented. These solutions were obtained by varying the 1st order dissipation coefficient from 0.25 to 0.125. It is shown that the reduction of the 1st order dissipation coefficient can give results closer to inviscid conditions.

The transonic sample flow solution with values 0.125 and 0.0015 for the dissipation coefficients, $k^{(2)}$ and $k^{(4)}$ revealed the shock capturing capability of the method described here. This was illustrated by plotting the pressure coefficient, Mach number, and entropy contours on the upper and lower surfaces of the cylinder (see Fig. 9).

There are numerous sources that can affect a numerical solution. These may include the local time stepping used with the time marching scheme, or the Courant numbers (CFL) used for the implicit residual smoothing. To consider only the effect of dissipation terms on the numerical flow solutions, Courant numbers were kept the same for local time stepping and residual smoothing was not employed. It was shown that proper adjustment of dissipation coefficients, $k^{(2)}$ and $k^{(4)}$ is required for every solid boundary shape considered. Furthermore, any change in the flow conditions such as the free stream Mach number, require new dissipation constants. It is, therefore, concluded that by adjusting the values of dissipation coefficients, $k^{(2)}$ and $k^{(4)}$ accurate Euler flow solutions can be obtained.

References:

- [1] MacCormak, R. W., and Baldwin, B. S., "A Numerical Method for Solving the Navier-Stokes Equations with Application to Shock-Boundary Layer Interaction", *AIAA Paper 75-1*, 1975.
- [2] Hirsch, C., "Numerical Computation of Internal and External Flows", Vol. 2: *Computational Methods for Inviscid and Viscous Flows*, John Wiley and Sons, New York, USA, 1992.

- [3] Steger J. L., "Implicit Finite Difference Simulation of Flow about Two-Dimensional Geometries", *AIAA Journal*, 16, 679-86, 1978.
- [4] Jameson, A., Schmidt, W., and Turkel, E., "Numerical Simulation of the Euler Equations by Finite Volume Methods Using Runge-Kutta Time Stepping Schemes", *AIAA 5th Computational Fluid Dynamics Conference*, 81-1259, 1981.
- [5] Jameson, A., "Transonic Aerofoil Calculations Using The Euler Equations", In P. L. Roe (editor), *Numerical Methods in Aeronautical Fluid Dynamics*, Academic Press, New York, USA, 1982.
- [6] Jameson, A., Baker, T. J., and Weatherill, N. P., "Calculation of Inviscid Transonic Flow Over a Complete Aircraft", *AIAA Paper 86 - 0103*, 1986.
- [7] Stolsis, L. and Johnston, L. J., "Solution of the Euler Equations on unstructured grids for Two-Dimensional Compressible Flow", *Aeronautical Journal*, Volume 94, pages 181-195, 1990.
- [8] Jameson, A., and Mavriplis, D., "Finite Volume Solution of the Two-Dimensional Euler Equations on a Regular Triangular Mesh", *AIAA Journal*, Vol. 24, No. 4, April 1986.
- [9] Schlichting, H., *Boundary Layer Theory*, 7th edition, McGraw Hill Book Co., NY, NY, 1987.
- [10] Bahrainian, Seyed Saied, Daneh Dezfuli, Alireza, An Unstructured Grid Generation Approach for Inviscid Flow Solutions, *WSEAS Transactions on Fluid Mechanics*, Issue 1, Vol. 4, pp 24-33, 2009.
- [11] Bahrainian, S. S., Construction of Hexahedral Block Topology and its Decomposition to Generate Initial Tetrahedral Grids for Aerodynamic Applications, *Journal of Aerospace, Science, and Technology (JAST)*, Vol. 5, No. 2, pp 81-90, 2008.

$E, F, G, W,$	vectors
$F,$	flux vector
$H,$	total enthalpy
$L,$	length or span
$k^{(2)}, k^{(4)}$,	adjustable dissipation coefficients
$M,$	Mach number
$n,$	unit outward normal vector
$P,$	static pressure
$\mathbf{R},$	vector of residuals
$R,$	Riemann invariant
$s,$	entropy
$T,$	temperature
$u, v, w,$	Cartesian velocity components
$\alpha,$	angle of attack
$\Omega,$	control volume, cell volume, volume
$\varepsilon^{(2)},$	1st - order pressure switches
$\varepsilon^{(4)},$	3rd - order pressure switches
$v_i,$	pressure sensor for cell i
$\gamma,$	ratio of specific heats
$\rho,$	density
$\Delta t,$	time step
$W,$	vector of independent variables
$w_1, \dots, w_5,$	components of the unknown vector
$\Delta x, \Delta y,$	spatial increment in x and y directions

Nomenclature

$A,$	cell area
$c,$	speed of sound, chord
$c_p,$	specific heats at constant pressure
$c_v,$	specific heats at constant volume
$C_p,$	pressure coefficient
$\mathbf{D},$	artificial dissipation vector, diameter
$E,$	total energy per unit mass or volume